STRUCTURAL BIOLOGY

Cryo-EM structures of excitatory amino acid transporter 3 visualize coupled substrate, sodium, and proton binding and transport

Biao Qiu[1], Doreen Matthies[2]*, Eva Fortea[1], Zhiheng Yu[2], Olga Boudker[1,3]†

Human excitatory amino acid transporter 3 (hEAAT3) mediates glutamate uptake in neurons, intestine, and kidney. Here, we report cryo-EM structures of hEAAT3 in several functional states where the transporter is empty, bound to coupled sodium ions only, or fully loaded with three sodium ions, a proton, and the substrate aspartate. The structures suggest that hEAAT3 operates by an elevator mechanism involving three functionally independent subunits. When the substrate-binding site is near the cytoplasm, it has a remarkably low affinity for the substrate, perhaps facilitating its release and allowing the rapid transport turnover. The mechanism of the coupled uptake of the sodium ions and the substrate is conserved across evolutionarily distant families and is augmented by coupling to protons in EAATs. The structures further suggest a mechanism by which a conserved glutamate residue mediates proton symport.

INTRODUCTION

Human excitatory amino acid transporters (hEAATs) pump glutamate into cells against steep concentration gradients by using the pre-established inward-directed sodium and proton transmembrane gradients and outward-directed potassium gradients as an energy source (*1*, *2*). hEAAT3 is one of five human EAAT subtypes broadly expressed in neurons throughout the brain. It is the major glutamate and aspartate transporter outside of the central nervous system, including kidneys and intestines (*3*–*5*). EAAT3 knockout in mice and loss-of-function mutations in hEAAT3 cause dicarboxylic aminoaciduria, a metabolic disorder that leads to the excessive loss of aspartate and glutamate in the urine (*6*, *7*). Notably, the disorder can be associated with mental retardation and obsessive-compulsive syndrome (*8*).

EAAT3 is expressed in the somata and dendrites of both excitatory and inhibitory neurons in the mammalian brains but excluded from presynaptic membranes. EAAT3 total levels in the brain are approximately 100 times lower than EAAT2 (*9*), which mediates most of the glutamate uptake following synaptic transmission (*10*). Nevertheless, altered EAAT3 expression and plasma membrane trafficking are associated with epilepsy, schizophrenia, and hypoxia; decreased activity leads to neuron susceptibility to oxidative damage, particularly in epilepsy models (*11*–*14*). The relevance of EAAT3 to oxidative stress resistance might be due to its ability, unique among EAATs, to transport cysteine, which is a rate-limiting intermediate in the biosynthesis of the antioxidant glutathione (*15*–*17*). Thus, activators of hEAAT3 might be useful to boost cysteine uptake into neurons under pathologic conditions. Because of the high concentration of glutamate in neurons, hEAAT3 might also run in reverse during ischemia, spilling excitotoxic levels of glutamate into the extracellular space. Therefore, specific inhibitors of hEAAT3 might be clinically helpful in reducing glutamate-mediated damage following transient ischemic conditions and depolarization of membranes.

A detailed understanding of the hEAAT3 structure and mechanism would be required to enable pharmacologic manipulations. Moreover, EAAT3 is one of the best functionally characterized glutamate transporters, making it an excellent target for structural studies. Thus, we determined the structures of hEAAT3 using cryo–electron microscopy (cryo-EM). The transporter is a homotrimer with each protomer consisting of two domains, a central trimerization scaffold, and a peripheral transport domain containing the substrate-binding site. The individual hEAAT3 protomers undergo elevator-like transitions between the outward- and inward-facing conformations, in which their transport domains localize closer to the extracellular space and the cytoplasm, respectively. We observe trimers with every possible arrangement of the outward- and inward-facing protomers, consistent with protomer independence. When we imaged hEAAT3 in the presence of aspartate and sodium ions, we observe that only outward-facing protomers bound the amino acid, while inward-facing protomers remained substrate-free. We conclude that the substrate-free transporter has a strong preference for the inward-facing conformation, while the outward-facing transporter has a substantial higher affinity for the amino acid. Last, we compare the transport domain structures when free of ligands, bound to sodium ions, and bound to sodium ions, protons, and aspartate. These structures provide mechanistic insights into the symport of the amino acid, sodium, and protons in hEAAT3.

RESULTS

The elevator mechanism of hEAAT3

We heterologously expressed and purified full-length hEAAT3, with two potential glycosylation sites mutated (N178T and N195T), $hEAAT3_g$ (fig. S1, A to C). The wild type and mutant showed aspartate uptake in oocytes with similar K_m (Michaelis constant) values of 39 ± 7 and 63 ± 11 μM (Fig. 1A), suggesting that mutations do not significantly alter the function of the transporter. The purified,

[1]Department of Physiology and Biophysics, Weill Cornell Medicine, 1300 York Ave, New York, NY 10021, USA. [2]Howard Hughes Medical Institute, Janelia Research Campus, 19700 Helix Drive, Ashburn, VA 20147, USA. [3]Howard Hughes Medical Institute, Weill Cornell Medicine, 1300 York Ave, New York, NY 10021, USA.
*Present address: Unit on Structural Biology, Division of Basic and Translational Biophysics, Eunice Kennedy Shriver National Institute of Child Health and Human Development, National Institutes of Health, Bethesda, MD 20892, USA.
†Corresponding author. Email: olb2003@med.cornell.edu

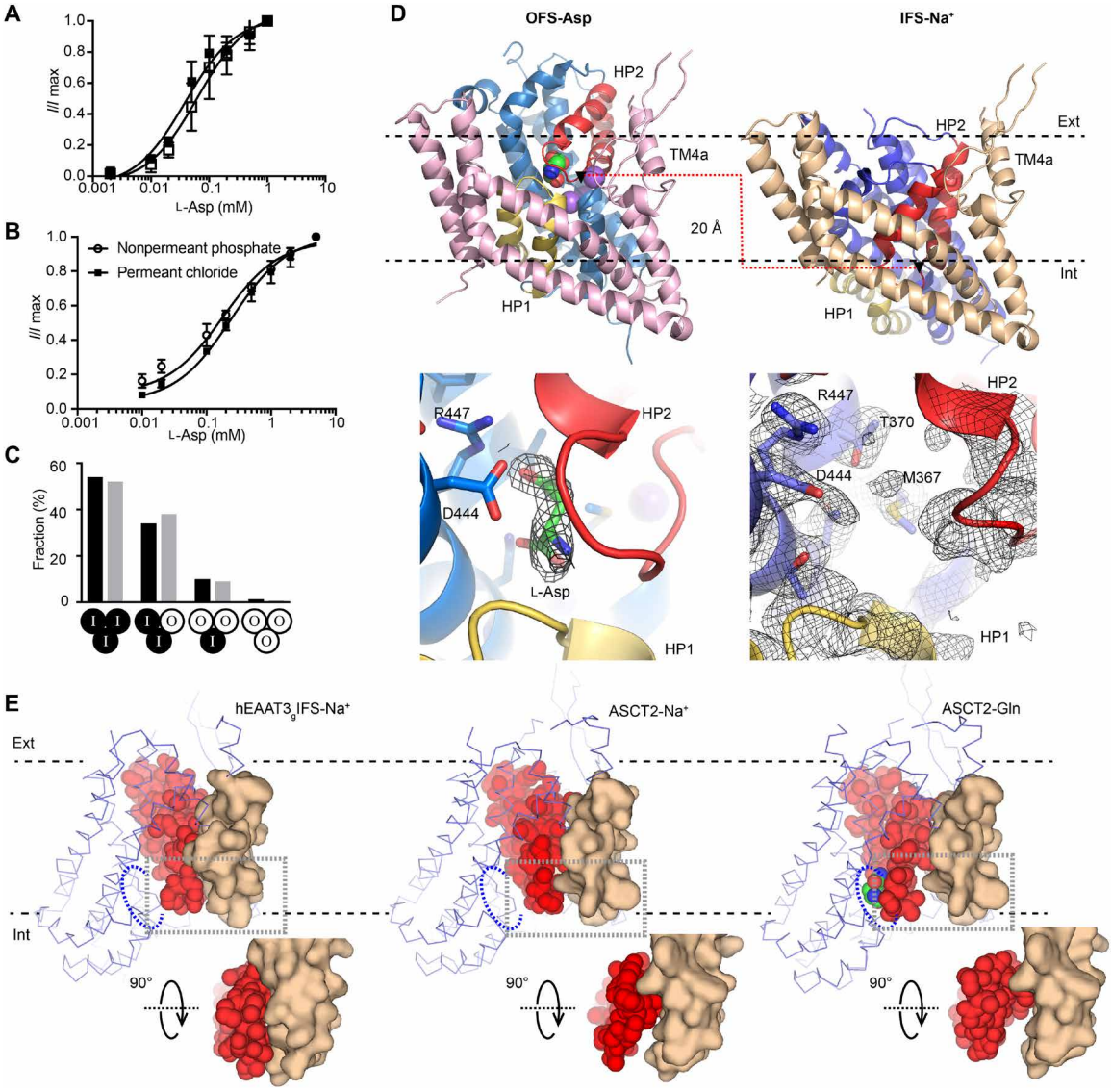

Fig. 1. Alternating access mechanism of hEAAT3$_g$. (**A**) hEAAT3$_g$ (open squares) and wild-type hEAAT3 (solid squares) show similar L-asp uptake in oocytes. Measured currents are plotted as fractions of the maximal observed current. (**B**) Transient currents mediated by hEAAT3$_g$ reconstituted into solid-supported membranes. Measured peak currents are plotted as fractions of the maximal observed peak current. Currents were measured in buffers containing nonpermeant phosphate (open circles) and permeant chloride (solid squares) anions. (**C**) Observed populations of hEAAT3$_g$ trimers with different configurations of protomers in the OFS (O) and IFS (I), as indicated below the graph (black columns), are consistent with binomial distributions with OFS probability of 19% (gray columns). The analysis is based on the cryo-EM imaging data for hEAAT3$_g$ in the presence of 200 mM NaCl and 1 mM L-asp. (**D**) Structures of single hEAAT3$_g$ protomers in the IFS-Na^+ (left) and OFS-Asp (right) states. The scaffold domains are pink and beige, and the transport domains are in shades of blue. Structurally symmetric HP1 and HP2 are yellow and red, respectively. Substrate and ions are shown as spheres and colored by atom type. Below are the close-up views of the substrate-binding sites. The gray mesh objects are density maps contoured at 5.5 σ for L-asp (left) and 4.5 σ for the protein (right). (**E**) Interactions between HP2 (red spheres) and scaffold domain (beige surface) for the inward-facing hEAAT3$_g$ bound to Na^+ ions (left), ASCT2 bound to Na^+ ions [Protein Data Bank (PDB) accession code 6rvx, middle], and ASCT2-Gln bound to glutamine (PDB accession code 6gct, right). Dotted blue ellipses highlight the locations of the substrate-binding site for reference. The rest of the transport domains are shown as blue ribbons. The close-up views are below the panels.

liposome-reconstituted hEAAT3$_g$ showed electrogenic aspartate uptake in solid-supported membrane (SSM) electrophysiology assays (fig. S1, D to G). The uptake required a sodium (Na^+) ion gradient and was inhibited by (3*S*)-3-[[3-[[4-(trifluoromethyl)benzoyl]amino]phenyl]methoxy]-L-aspartic acid (TFB-TBOA) (fig. S1, D and E). All EAATs, including hEAAT3, show thermodynamically uncoupled anion conductance gated by glutamate or aspartate binding (*18*–*22*). We found that hEAAT3$_g$-mediated transient currents in SSM experiments comprised a positive peak and a negative overshoot in the presence of a permeant anion (chloride); only positive currents remained when chloride was replaced by impermeant phosphate (fig. S1, F and G). These observations suggest that the purified hEAAT3$_g$ retains both coupled transport and uncoupled channel activities. The apparent aspartate K_m values were 179 ± 23 and 242 ± 24 μM in the absence and presence of the permeant anion, respectively (Fig. 1B). These values are higher than in oocytes

and mammalian cells (*23*–*25*). The discrepancies might reflect distinct lipid environments. Furthermore, hEAAT3 showed a significantly higher K_m of reverse transport (*26*, *27*). Thus, it is possible that in the reconstructed system with the mixed orientations of the transporter, a combination of the forward and reverse transport is observed, yielding a higher observed K_m than in cell assays.

We first acquired cryo-EM micrographs of $hEAAT3_g$ in the presence of 200 mM NaCl and 1 mM L-aspartate (L-asp). In these studies, we used aspartate rather than glutamate because the transporter has a higher affinity for the former. Following two-dimensional (2D) and 3D classifications, 3D refinement with applied C3 symmetry yielded a density map with an overall resolution of 2.85 Å (table S1 and figs. S2, A to C, and S3A). The trimeric transporter showed an overall architecture (fig. S4) similar to those of the homologous archaeal transporters Glt_{Ph} and Glt_{Tk} (*28*–*31*), a thermostabilized variant of human EAAT1 (htsEAAT1) (*32*), and human neutral amino acid transporter ASCT2 (*33*, *34*). The central trimerization scaffold supported three peripheral transport domains in inward-facing states (3i). Although the scaffold domain is more divergent than the transport domain, its overall architecture and many residues involved in inter-subunit interactions are well conserved (fig. S5). All family members feature a large, similarly sized, lipid- or detergent-filled cavity on the trimeric symmetry axis. Highly conserved V155 and F159 in transmembrane segment 4b (TM4b) and F239 in TM5 seal the cavity in hEAAT3g from the extracellular and intracellular sides, respectively. The insertions of variable sizes between TM4b and TM4c feature the most striking sequence divergence in the family. The inserted loop is the shortest in ASCT2 and is fully resolved in the cryo-EM maps. It mostly comprises two antiparallel β strands and looks like an arm rising above the transporter's extracellular rim. While the arm extends over the neighboring subunit, it contributes little to the assembly and interacts mostly with the scaffold TM4a of its own protomer. The role of this structure is unclear. Despite sequence differences, the resolved part of the hEAAT3g loop is structurally similar to ASCT2. The loop is significantly longer in hEAAT3 and contains the mutated glycosylation sites. However, these regions are flexible and unresolved in our structures.

Unexpectedly, symmetry expansion revealed ~19% subpopulation of protomers in an outward-facing conformation (fig. S2). We refined these protomers to 3.03-Å resolution (table S1 and fig. S3B). We then sorted 554,920 particles of EAAT3 trimers based on the conformations of their protomers and estimated the fractions containing three (3i), two (2i1o), one (1i2o), and zero (3o) inward-facing protomers. These were in good agreement with the binomial distribution (Fig. 1C). Using these sorted trimers, we refined the asymmetric 2i1o trimer and the symmetric 3i trimer to 3.42-Å (table S1 and fig. S3C) and 3.03-Å resolution, respectively. The map of the "purified" symmetric 3i trimer was virtually indistinguishable from the map obtained from all particles combined but was of slightly lower resolution. Lack of resolution improvement suggested that there might be additional structural heterogeneity. However, further symmetry expansion on the particles failed to reveal different conformational states. Together, these results show that transport domains sample outward- and inward-facing orientations independently of each other, consistent with the body of literature (*35*–*37*).

In the outward- and inward-facing protomers, the scaffold domain remained mostly unchanged. In contrast, the transport domain moved by ~20 Å from an extracellular to an intracellular position enabled by the interdomain hinges (Fig. 1D). The outward-facing protomers were bound to L-asp (OFS-Asp), while the inward-facing protomers were not (Fig. 1D). In the inward-facing protomers (IFS-Na^+), Na^+ ions likely occupy at least one of the three binding sites (discussed below), and we observe a characteristic opening of the helical hairpin 2 (HP2) proposed to gate the substrate-binding site (*38*–*40*). These results suggest that in the absence of transmembrane electrochemical gradients and substrate, $hEAAT3_g$ strongly favors the inward-facing conformation, similar to the archaeal Glt_{Tk} (*38*). Furthermore, inward-facing $hEAAT3_g$ has a remarkably low substrate affinity, at least under our imaging conditions. The substrate-bound protomers should be a minority at 1 mM L-asp and might be averaged out during processing, suggesting that the dissociation constant is above 1 mM. By contrast, all outward-facing protomers are bound to aspartate and $hEAAT3_g$ K_m, which is an approximation of the outward-facing dissociation constant, is ~60 μM. Thus, $hEAAT3_g$ is very different from the archaeal Glt_{Ph}, for which we measured similar high substrate affinities in both the outward- and inward-facing states under symmetric ionic conditions (*41*).

It is unlikely that the differences in substrate affinities in the OFS and IFS are due to different substrate coordination or local electrostatic potentials. Consistently, in ASCT2 and Glt_{Ph}, the substrate coordination is identical in the two states (*29*, *30*, *33*, *34*). Instead, we think that the differences in affinities are due to different conformations and structural environments of HP2 before L-asp binds. In the inward-facing substrate-free $hEAAT3_g$ and ASCT2, we observed the transport domains leaning away similarly from HP2, which remains in contact with the scaffold (Fig. 1E). In this manner, the binding site is open to the cytoplasm. Upon substrate binding to the inward-facing ASCT2, the tip of HP2 closes over the binding pocket (*33*, *40*). We expect that substrate binding and occlusion in $hEAAT3_g$ occurs by a similar mechanism. However, the HP2 tip is more extensively engaged with the scaffold in $hEAAT3_g$ than in ASCT2 (Fig. 1E), perhaps explaining, at least in part, its low affinity for the substrate.

Distinct mode of substrate binding to hEAAT3

The substrate-binding site geometry in $hEAAT3_g$ OFS-Asp resembles that of the archaeal homologs and htsEAAT1, but the L-asp side chain takes a different rotamer and is coordinated differently in $hEAAT3_g$ (Fig. 2, A and B, and fig. S6A). The main-chain carboxylate of L-asp is coordinated principally by $N451_{401}$ (here and elsewhere, the corresponding residue number in Glt_{Ph} is shown as the subscript for reference) in TM8 and $S333_{278}$ in HP1, similar to other homologs (*29*, *32*). In contrast, the side-chain carboxylate and the amino group of L-asp are coordinated differently. Carboxyl oxygens (OD1 and OD2) form hydrogen bonds with $R447_{397}$ in TM8, the main-chain amides of HP2 (OD1), and $T370_{314}$ in TM7 (OD2) in the archaeal transporters and htsEAAT1. However, in $hEAAT3_g$, the carboxyl group and $R447_{397}$ face away from each other somewhat. While still hydrogen-bonded by the guanidinium group, the carboxylate appears to be more engaged with $T370_{314}$ (Fig. 2A). L-Asp amino group in other homologs is coordinated primarily by the highly conserved $D444_{394}$ in TM8, but in $hEAAT3_g$, it is coordinated only by the carbonyl oxygens in HP1 and HP2. $D444_{394}$ does not interact with L-asp and, instead, interacts with $R447_{397}$. The structural basis of why the substrate binds differently to $hEAAT3_g$ remains unclear because the residues forming the binding site are

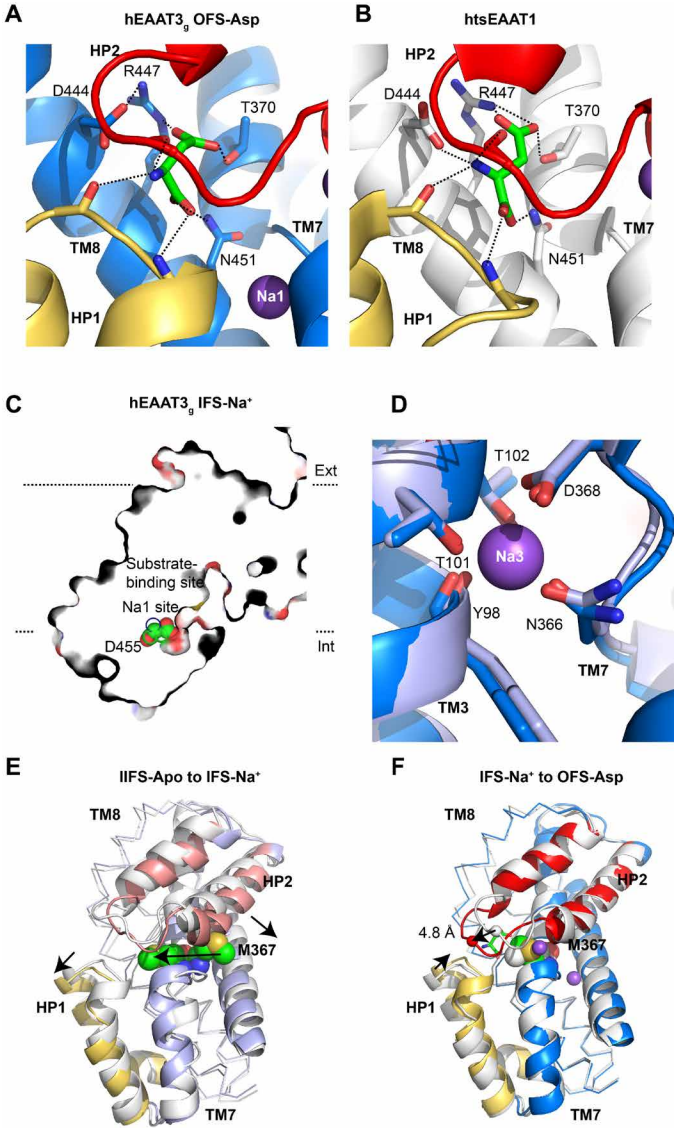

Fig. 2. Substrate and sodium coupling in hEAAT3$_g$. L-Asp binds differently to hEAAT3$_g$ (**A**) and thermally stabilized human EAAT1 (htsEAAT1, PDB accession code 5 lm4) (**B**). While the electron density for L-asp is a little ambiguous in htsEAAT1 structure, the substrate position and coordination is identical to Glt$_{Ph}$ and Glt$_{Tk}$, lending confidence to the model. Interactions between L-asp and EAATs are shown as dashed lines. HP1 and HP2 are colored yellow and red, respectively; L-asp is colored green; and TM7 and TM8 are colored blue (hEAAT3$_g$) and white (htsEAAT1), respectively. (**C**) Na1 is solvent accessible. hEAAT3$_g$ is shown as a thin slice taken through the Na1 site. The Na^+-coordinating residue D455 is shown as spheres and colored by atom type. (**D**) Close-up view of the Na3 site in hEAAT3$_g$ OFS-Asp (marine) and IFS-Na^+ (light blue). (**E** and **F**) Conformational changes within the transport domains transitioning from the IFS-Apo to IFS-Na^+ state (E) and IFS-Na^+ to OFS-Asp state (F). The transport domains are white and shades of blue for the starting and ending states, respectively, with HP1 in yellow and HP2 in salmon. M367 is shown as spheres and colored by atom type in all states. The arrows indicate conformational changes from IFS-Apo to IFS-Na^+ (E) and IFS-Na^+ to OFS-Asp (F).

highly conserved and essential for transport (*25*, *42*, *43*). Reduced reliance on R447$_{397}$ and coordination of the arginine by D444$_{394}$ might explain why hEAAT3 accepts cysteine as a substrate, while the other homologs do not.

Na^+ and substrate coupling

All sodium-coupled glutamate transporters with known ionic stoichiometry symport their substrates with three sodium ions (*23*, *44*–*46*). We observed density corresponding to Na^+ ions at all three conserved Na^+-binding sites Na1, Na2, and Na3 in the OFS-Asp protomer (fig. S6, B to D). In the IFS-Na^+ protomers, L-asp and Na2 sites are distorted and empty because of the open HP2. The coordinating groups of the Na1 site below the substrate-binding site are in place, but we did not observe any density for the ion. Moreover, it appears that the site, in particular, the critical D455$_{405}$ residue, is solvent accessible (Fig. 2C). Na3 site is located deep in the protein core. All coordinating residues are in place, and the site is likely occupied, although ion density is unresolved (Fig. 2D). These results are consistent with previous suggestions that the Na3 site has the highest affinity and might be the first to bind the ion (*31*, *47*, *48*). In contrast, the Na1 site might be in rapid exchange with the bulk solution and remain only partially occupied at 200 mM Na^+ ions used during grid preparation.

Substrate binding to glutamate transporters, both archaeal and human, is sodium dependent (*29*, *49*, *50*). To uncover the structural basis of this dependence in hEAAT3$_g$, we wanted to compare hEAAT3$_g$ structures in the presence and absence of Na^+. Therefore, we imaged the transporter under apo conditions in a buffer containing 100 mM choline chloride. Following data processing, we only observed inward-facing symmetric trimers (IFS-Apo), which we refined to 3.03-Å resolution (table S1 and fig. S3D). The overall architecture of IFS-Apo protomers is similar to IFS-Na^+, but the transport domains swing further away from the scaffold and shift outward slightly. The IFS-Apo and IFS-Na^+ transport domains superimposed with an overall root mean square deviation (RMSD) of 1.3 Å, with the most significant conformational changes in TM7 and HP2 (Fig. 2E). In further considering the mechanism of coupling between sodium and aspartate binding, we took advantage of the observations that the conformational changes upon ion and substrate binding are confined to transport domains and similar in the outward- and inward-facing states of glutamate transporters (*38*, *39*, *51*). Therefore, we compared the transport domains of IFS-Apo, IFS-Na^+, and OFS-Asp to visualize structural events during binding.

We observed that a critical structural change upon binding of Na^+ ions to the apo protein is the repositioning of M367$_{311}$, part of the highly conserved Asn-Met-Asp motif in TM7. When Na^+ ions bind to Na1 and Na3 sites, coordinated, in part, by N366$_{310}$, M367$_{311}$ side chain flips from pointing into the lipid bilayer to pointing toward the substrate-binding site, where it also contributes to the Na2 site (Fig. 2E) (*31*). The flipped-out M367$_{311}$ side chain, as seen in IFS-Apo, would sterically clash with the closed HP2 conformation observed in the OFS-Asp, perhaps disfavoring L-asp binding in the absence of the ions (Fig. 2, E and F). Once Na^+ ions bind to Na1 and Na3 sites, M367$_{311}$ and HP2 are repositioned in a manner compatible with substrate binding, which causes only minimal further structural changes, limited to the closure of HP2 and the formation of the Na2 site (Fig. 2F). Striking similar movements of the corresponding M311 residue contribute to the coupled binding in Glt$_{Ph}$ (*29*, *51*), suggesting that the mechanism is conserved in glutamate transporters of vastly different evolutionary origins.

HP2 is open in the IFS-Apo of hEAAT3$_g$. Previously, both open and closed HP2 conformations were visualized in inward-facing Glt$_{Ph}$ (*39*, *51*), and both Glt$_{Ph}$ and Glt$_{Tk}$ display closed HP2 conformations in the apo outward-facing states (*31*, *51*–*53*). Closure of HP2 is thought to be required for the rapid transmembrane movements

of the transport domain. In human EAATs, potassium binding might be necessary to close HP2, ensuring coupled potassium antiport. We speculate that the inability of $hEAAT3_g$ IFS-Apo to close HP2, contrasting it to the archaeal homologues, is related to the $R447_{397}$ side-chain position. In the apo archaeal transporters, $R447_{397}$ moves into the substrate-binding site where it can form direct or through-water hydrogen bonds with the main-chain carbonyl oxygens of the HP2 tip. In $hEAAT3_g$ IFS-Apo, $R447_{397}$ interacts with the TM7 residue $E374_{318}$ (glutamine in archaeal homologs) and is not available to close HP2 (fig. S7, A and B). An $R447_{397}$-$E374_{318}$ salt bridge might also sterically hinder HP2 closure (*54*). Recent work suggests that the potassium binding site in EAATs might be located between the Na1 and Na3 sites (*54*) or overlap with the Na1 site (*55*). Unfortunately, we were unable to visualize potassium binding to $hEAAT3_g$ because the cryo-EM structure obtained in the presence of 250 mM KCl (fig. S3E) looks identical to IFS-Apo with overall RMSD of 0.36 Å. Both Na1 and Na3 sites are distorted in the IFS-Apo conformation in the absence and presence of potassium, and we do not see excess densities that could correspond to a potassium ion.

Gating coupled to proton binding

The working cycle of EAATs involves the symport of a proton along with the amino acid and Na^+ ions. $E374_{318}$ in EAAT3 and the equivalent residues in other EAATs might be the proton acceptors, and mutating them to glutamines resulted in substrate translocation only in an exchange mode (*56*). Consistently, in archaeal homologs and ASCT2, which are not proton-coupled, $E374_{318}$ is replaced by a glutamine. Furthermore, mutating $R447_{397}$ in EAAT3 to cysteine abolished aspartate and glutamate transport but allowed cysteine transport in an exchange mode, suggesting that R447 is also involved in proton coupling (*42*). In OFS-Asp $hEAAT3_g$, $E374_{318}$ is occluded from the solution by HP2 and makes no interactions with other residues (Fig. 3, A and D). $R447_{397}$ interacts with $D444_{394}$ and with $Y373_{317}$ through a cation-π interaction. In IFS-Na^+, HP2 is open, and $E374_{318}$ is positioned at the far end of a cavity, where it forms a hydrogen bond with $T418_{362}$ (Fig. 3, B and E). Conformations of $R447_{397}$ and other substrate-coordinating residues (S333, T370, and N451) are almost the same as in OFS-Asp. Last, in IFS-Apo, the side chains of $R447_{397}$ and $E374_{318}$ flip towards each other to form a salt bridge (Fig. 3, C and F). The interaction between $R447_{397}$ and $Y373_{317}$ breaks and $R447_{397}$ descends into the substrate-binding site. Thus, R447 interacts with either substrate or E374 as previously suggested (*57*). We calculated the pK_a (where K_a is the acid dissociation constant) values of $E374_{318}$ in the apo, Na^+-bound, and L-asp–bound states using PROPKA (*58*). The obtained values of 7.7, 7.5, and 8.5, respectively, were similar to the experimentally measured pK_a values for proton binding to EAAT3 (*26*). Increased pK_a values and occlusion from solvent suggest that $E374_{318}$ is more

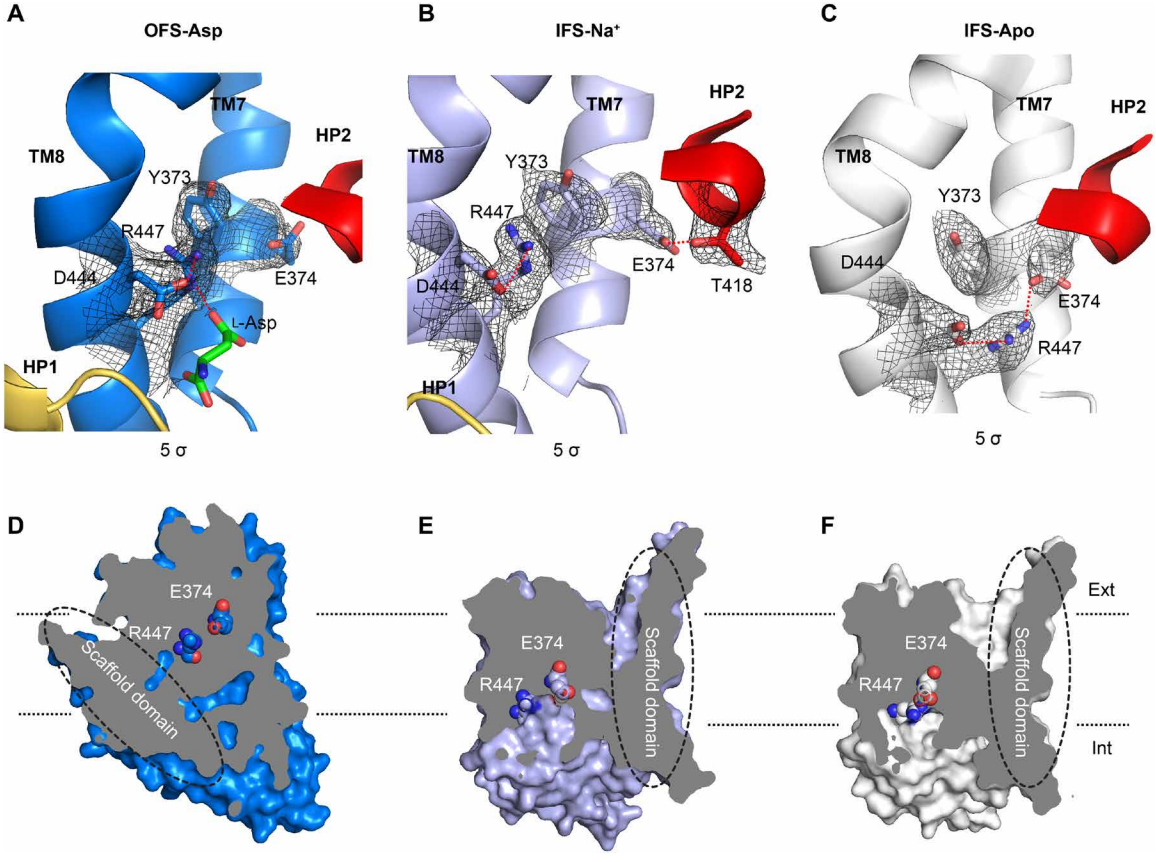

Fig. 3. The proton coupling mechanism of $hEAAT3_g$. Close-up views of R447 and E374 in the OFS-Asp state (**A**), IFS-Na^+ state (**B**), and IFS-Apo state (**C**). Key interactions are shown as red dashed lines; density of residues is shown as mesh; the contour levels of the maps are below the panels. HP1 and HP2 are yellow and red, respectively. TM7 and TM8 are marine, light blue, and white in (A), (B), and (C), respectively. L-Asp is green. Position of R447 and E374 relative to the membrane and their solvent accessibility in the OFS-Asp state (**D**), IFS-Na^+ (**E**), and IFS-Apo state (**F**). hEAAT3g is shown as a surface sliced approximately through the substrate-binding site and viewed in the membrane plane. Dashed ellipses mark the scaffold domains. R447 and E374 are shown as spheres.

likely to bind protons when Na^+ ions and L-asp bind to the transporter. In this manner, the binding of protons, Na^+ ions, and the substrate is coupled. Consistently, molecular dynamics simulations showed that the protonation of E374 could favor ligand binding (*59*). During the return of the apo transport domain from the inward- into the outward-facing state, the $E374_{318}$-$R447_{397}$ salt bridge would allow the occlusion of the deprotonated residue.

DISCUSSION

EAAT3 is the fastest EAAT subtype with turnover times of ~10 ms (*1*, *60*). Like other members of the family, it operates by an elevator mechanism. The movements of the individual transport domains within the trimer are independent of each other, leading to a stochastic distribution of the outward- and inward-facing protomers observed in cryo-EM imaging experiments. We find that the affinity of the inward-facing state is low, and all observed inward-facing protomers are substrate-free in 1 mM aspartate. In contrast, the substrate affinity of the outward-facing state is much higher, and all outward-facing protomers showed the bound substrate. In that regard, $hEAAT3_g$ differs from the archaeal Glt_{Ph}, which showed comparable aspartate affinities in the outward- and inward-facing states (*41*). Thus, our data suggest that during the transport cycle of EAAT3, the inward-facing substrate-bound closed state is a transient, unstable state and that the release of the substrate is rapid. We further speculate that potassium-bound inward-facing closed conformation might also be a comparatively high-energy state, perhaps explaining why we did not observe it in our imaging experiments. This hypothesis is consistent with the reorientation of the potassium-bound transport domain being the rate-limiting step of the transport cycle (*60*).

Our data, together with the published work, suggest that a two-prong structural mechanism of Na^+ and amino acid symport is conserved in evolution from archaea to humans. First, binding of Na^+ ions to the Na1 and Na3 sites is a prerequisite for the binding of substrate and Na^+ in the Na2 site and leads to movements of two critical residues: $R447_{397}$ out of the binding site to make space for the amino acid, and $M367_{311}$ into the binding site, where it coordinates Na^+ in the Na2 site. Second, uncoupled transport of Na^+ ions bound to Na1 and Na2 sites is prevented because the closure of the HP2 tip, essential to allow translocation, requires binding of the substrate and Na^+ in the Na2 site. Thus, HP2 is open in the IFS-Na^+ structure, likely hindering transport domain movements. In EAATs, the coupling to $E374_{318}$ protonation enhances the mechanism. Breaking of the interaction between $E374_{318}$ and $R447_{397}$, favored by $E374_{318}$ protonation, is necessary to make the arginine available to coordinate the substrate. Furthermore, the protonation of $E374_{318}$ is likely required to allow HP2 closure, which completely occludes the residue in a nonpolar protein interior.

MATERIALS AND METHODS

Protein expression and purification

The codon-optimized full-length human EAAT3 was cloned into a modified pCDNA 3.1 (+) plasmid (Invitrogen), which has N-terminal Strep·Tag II followed by an enhanced green fluorescent protein (eGFP) and PreScission protease site. Glycosylation sites, N178 and N195, were mutated to threonines by site-directed mutagenesis. Human embryonic kidney (HEK) 293F cells (Invitrogen) at a density of 2.5×10^6 cells/ml cultured in the FreeStyle293 medium (Gibco) were transiently transfected using 3 mg of appropriate plasmid using poly-ethylenimine (PEI) (Polysciences) as a 1:3 plasmid to PEI weight ratio. The cells were diluted with an equal volume of fresh FreeStyle293 medium 6 hours following the transfection, and valproic acid (Sigma-Aldrich) was added to a final concentration of 2.2 mM to boost protein expression 12 hours later. The cells were collected ~48 hours after transfection by centrifugation at 4000*g* for 10 min at 4°C. Cell pellets were resuspended in buffer containing 50 mM tris-Cl (pH 8.0), 1 mM L-asp, 1 mM EDTA, 1 mM tris(2-carboxyethyl) phosphine (TCEP), 1 mM phenylmethylsulfonyl fluoride (PMSF), and 1:200 dilution of mammalian protease inhibitor cocktail (Sigma-Aldrich). The resuspended cells were disrupted using an EmulsiFlex-C3 cell homogenizer (Avestin) or flash-frozen by liquid nitrogen and stored at −80°C for further use. Cell debris was removed by centrifugation at 10,000*g* for 15 min at 4°C, and membranes were harvested by ultracentrifugation at 186,000*g* for 1 hour at 4°C. The membrane pellets were resuspended and homogenized using a Dounce homogenizer in buffer containing 50 mM tris-Cl (pH 8.0), 200 mM NaCl, 1 mM aspartate, 1 mM EDTA, 1 mM TCEP, 1 mM PMSF, 1:200 dilution of mammalian protease inhibitor cocktail, and 10% (v/v) glycerol. The membranes were incubated with 2% dodecyl-β-D-maltopyranoside (DDM; Anatrace) and 0.4% cholesteryl hemisuccinate (CHS; Sigma-Aldrich) for 1 hour at 4°C. After ultracentrifugation at 186,000*g* for 1 hour at 4°C to remove insoluble material, the supernatant was incubated with Strep-Tactin Sepharose resin (GE Healthcare) for 1 hour at 4°C. For the L-asp–containing samples, the resin was washed by eight-column volumes of buffer containing 50 mM tris-Cl (pH 8.0), 200 mM NaCl, 0.06% glyco-diosgenin (GDN; Anatrace), 1 mM TCEP, 5% glycerol (wash buffer), and 1 mM L-asp. Protein was eluted with four-column volumes of the wash buffer supplemented with 2.5 mM D-desthiobiotin (elution buffer). Strep·Tag II and eGFP were removed by incubating the protein with homemade PreScission protease at 100:4 protein to protease ratio at 4°C overnight. EAAT3 was further purified by size exclusion chromatography using Superose 6 10/300 column (GE Healthcare) pre-equilibrated with 20 mM tris-Cl (pH 8.0), 200 mM NaCl, 1 mM TCEP, 0.01% GDN (gel filtration buffer), and 1 mM L-asp. To prepare Na^+/L-asp–free samples, the protein was exchanged during size exclusion chromatography into a buffer containing 20 mM tris-Cl (pH 8.0), 1 mM TCEP, 0.01% GDN, and 250 mM KCl or 100 mM choline chloride.

EM data acquisition

To prepare grids for cryo-EM imaging, 3 to 3.5 μl of EAAT3 at ~6 mg/ml were applied to glow-discharged QF R1.2/1.3 300 mesh gold or 400 mesh copper grids (Quantifoil, Großlöbichau, Germany). Grids were blotted either for 3 s at 4°C and 100% set humidity and plunge-frozen into liquid ethane using FEI Mark IV Vitrobot (FEI Company, part of Thermo Fisher Scientific, Hillsboro, OR) or for 7 s using Leica EM GP (Leica Microsystems Inc., Buffalo Grove, IL). Grids were screened using an FEI Tecnai F20 transmission electron microscope operated at 200 kV through a Gatan 626 side-entry cryo holder equipped with a Gatan K2 Summit direct detector (Gatan Inc., Pleasanton, CA) or FEI Tecnai Spirit BioTWIN with a TVIPS F416 camera. The three cryo-EM datasets discussed here were collected at a 300-kV FEI Titan Krios cryo-EM (HHMI Janelia Krios2) using SerialEM (*61*, *62*). The microscope was equipped with a GIF Bioquantum energy filter and a post-GIF K3 camera (Gatan Inc.). A 100-μm C2 aperture, a 100-μm objective aperture, and a 20-eV energy

slit centered around the zero-loss peak were used during data collection. Dose fractionation (movie) data were collected at a nominal magnification of ×105,000, that is, calibrated magnification of ×60,096, corresponding to a physical pixel size of 0.832 Å/pixel (0.416 Å/pixel in the resultant movie data with a binning of 0.5× selected). With the K3 camera in standard (non-correlated-double sampling) counted mode, a dose rate of 15 e^-/pixel/s was used, and each movie contains 60 frames with a total accumulated dose of 60 $e^-/Å^2$ on the sample. A nominal defocus range between ~−0.5 and −1.5 μm was applied.

Data processing

For the dataset collected for EAAT3 in the presence of 1 mM L-asp, drift correction was performed using MotionCor2 (*63*), and the contrast transfer function (CTF) parameters of micrographs were estimated using Gctf (*64*). All other steps of image processing were performed in Relion 3.0 (*65*). A total of 1,717,667 particles were selected from 6178 micrographs using a box of 288 pixels. The extracted particles were binned by two and subjected to two rounds of 2D classification and one round of 3D classification. The 3D class showing a good secondary structure was selected, and the particles were re-extracted using the original pixel size of 0.832 Å.

After 3D refinement with C3 symmetry and postprocessing, the resulting 3D reconstruction from 554,920 particles yielded a map at a 2.85-Å global resolution. The particles after refinement were expanded using C3 symmetry, and an inverted mask generated using the inward-facing protomer was applied for signal subtraction (first signal subtraction). The resulting 1,664,760 protomers were subjected to 3D classification with a mask and without alignment. A total of 325,222 particles in an outward-facing state and 1,339,538 particles in an inward-facing state were selected. The following 3D refinement and postprocessing using the outward-facing particles yielded a map at 3.2-Å resolution. An inverted mask generated using the outward-facing protomer was applied to the expanded particles for a second-round signal subtraction. A total of 312,743 particles in an outward-facing conformation were selected after masked 3D classification without alignment. A final map at 3.03-Å resolution was obtained after 3D refinement and postprocessing.

We identified trimers with two inward- and one outward-facing protomer (2i1o) by analyzing the coordinates of the protomers generated by the first round of signal subtraction and 3D classification using a home-written script. In total, 190,599 trimers were extracted from the raw micrographs. The first round of refinement of the 2i1o particles yielded a map at 3.99-Å resolution. The refined particles were then subjected to an additional 3D classification. A total of 158,349 particles were selected and further refined, yielding the final 2i1o map at 3.42-Å resolution after postprocessing. Purified 3i particles were also extracted from raw micrographs and refined to 3.03 Å. Similar processing as the first signal subtraction was also performed on these particles; no other conformations were found.

Other datasets were processed in Relion 3.0. Drift correlation was performed using Motioncor2 within Relion 3.0, and CTF parameters of micrographs were estimated using CTFFIND (*66*). From the dataset collected for EAAT3 in KCl buffer, 1,769,994 particles were auto-picked and extracted with twofold binning from 7036 micrographs. A total of 668,093 particles were selected and re-extracted after two rounds of 2D classification and one round of 3D classification. A final map at 2.85-Å resolution was obtained after 3D refinement, postprocessing, and polishing. For the dataset collected in choline chloride buffer, 1,918,723 particles were auto-picked from 4473 micrographs, and 435,398 particles were selected and re-extracted. A map at 3.24-Å resolution was obtained after 3D refinement and postprocessing. Further CTF-refinement and postprocessing improved the map to 3.03 Å. Symmetry expansion with signal subtraction and 3D classification without alignment was also performed on all datasets as described above. No conformational heterogeneity was found.

Model building and refinement

Model building was carried out in COOT (*67*), and the protein models were refined using Phenix (*68*). For cross-validation, the final model was displaced and then refined against the first unfiltered half-map. fourier shell correlation (FSC) curves were calculated between the refined model and the first unfiltered half-map, the refined model and the second unfiltered half-map (which was not refined), and the refined model and the summed map (*69*). The well overlaid FSC curves of the two unfiltered maps indicated no overfitting. The structure figures were prepared in Chimera (*70*) or PyMOL (DeLano Scientific).

Proteoliposome reconstitution

Liposomes were prepared using 5:5:2 (w/w) ratio of 1-palmitoyl-2-oleoyl-*sn*-glycero-3-phosphocholine (POPC), 1-palmitoyl-2-oleoyl-*sn*-glycero-3-phosphoethanolamine (POPE; Avanti Polar Lipids), and CHS. The lipids in chloroform were dried and rehydrated at 20 mg/ml by 10 freeze-thaw cycles in buffer containing 50 mM Hepes-tris buffer (pH 7.4). The liposomes were diluted to 4 mg/ml in buffer containing 50 mM Hepes/NaOH (pH 7.4), 200 mM NaCl, 1 mM TCEP, and 1 mM L-asp and extruded 11 times through 400-nm polycarbonate membranes (Avanti Polar Lipids) using a syringe extruder (Avanti Polar Lipids) to form unilamellar liposomes. Liposomes were destabilized with DDM at a 1:1.5 (w/w) lipid to detergent ratio for 15 min at room temperature, and the purified EAAT3 protein was added to the mixture at a 1:10 (w/w) protein to lipid ratio for 30 min at room temperature. The detergent removal was carried out by adding Bio-Beads SM-2 (100 mg/ml) (Bio-Rad) for 30 min at room temperature followed by five additional rounds at 4°C. To exchange the internal buffer, the proteoliposomes were pelleted by ultracentrifugation at 100,000*g* for 45 min at 4°C, diluted into the desired buffer, and subjected to freeze-thaw. Centrifugation and freeze-thaw steps were repeated three times. The proteoliposomes were extruded 11 times through 400-nm polycarbonate membranes for immediate use.

SSM assay

The internal proteoliposome resting buffer contained 100 mM potassium phosphate (pH 7.4), 2 mM $MgSO_4$ (nonpermeant anion condition) or 50 mM Hepes/KOH (pH 7.4), 150 mM KCl, 2 mM $MgCl_2$ (permeant anion condition). The SF-N1 sensor with a 3 mm diameter (Nanion Technologies) was prepared according to the instrument manual. The transport-coupled current was recorded by a double-solution exchange method (*71*, *72*) on a SURFE2R N1 instrument (Nanion Technologies). Briefly, a nonactivating buffer containing 100 mM sodium phosphate (pH 7.4), 2 mM $MgSO_4$ (nonpermeant anion condition) or 50 mM Hepes/NaOH (pH 7.4), 150 mM NaCl, 2 mM $MgCl_2$ (permeant anion condition) was flown through the sensor at a flow rate of 200 μl/s to build the ionic gradients across the membranes of the proteoliposomes deposited on the sensor. The transport-coupled current was initiated by flowing nonactivating buffer supplemented with different concentrations of

the substrate (activating buffers). Last, the sensor was rinsed in a resting buffer to restore the sensor. The L-asp affinities hEAAT3$_g$ were measured using sensors from at least two independent proteoliposome preparations, and the data were fitted by the equation

$$I = I_{max}\frac{X}{K_m + X} + B$$

where I is the peak current measured in different substrate concentrations, I_{max} is the fitted maximum peak current, X is the substrate concentration, and B is the baseline offset. TFB-TBOA inhibition was carried out by adding the inhibitor to final concentrations of 10 or 3 μM to nonactivating buffer and activating buffer containing 100 μM L-asp. Following the recording of the transport current, the sensor was restored as described above.

cRNA preparation, voltage-clamp oocyte recordings, and analysis

Wild-type hEAAT3 and hEAAT3$_g$ were cloned in a pTLN vector and transcribed in vitro using the mMessage mMachine SP6 Kit (Thermo Fisher Scientific). *Xenopus laevis* oocytes were purchased from Ecocyte Bio Science (Austin, TX, USA), injected with 25 ng of complementary RNA (cRNA), and kept at 18°C in 50% Leibovitz medium, gentamicin (250 mg/liter), 1 mM L-glutamine, and 10 mM Hepes (pH 7.6). Glass microelectrodes were pulled with a resistance of 0.5 to 3 megohms and backfilled with 3 M KCl. Currents were recorded 48 hours for the wild type and 72 hours for hEAAT3$_g$ after injection in ND96 solution [96 mM NaCl, 2 mM KCl, 1.8 mM $CaCl_2$, 1 mM $MgCl_2$, 5 mM Hepes (pH 7.5)] using an OC-725C voltage-clamp amplifier (Warner Instruments, Hamden, CT). The data were acquired with the Patchmaster (HEKA Elektronik, Lambrecht, Germany) at 5 kHz, filtered with a Frequency Devices 8-pole Bessel filter at a corner frequency of 2 kHz, and analyzed using Ana (M. Pusch, Istituto di Biofisica, Genova) and Prism (GraphPad). The stimulation protocol for IV curves was as follows: From a holding potential of −30 mV, the voltage was stepped to a variable voltage in 20-mV incremental jumps from −100 mV to +60 mV for 200 ms and stepped back to −30 mV. For calculating K_m, a −100-mV pulse was applied for 200 ms at different ligand concentrations. Each concentration point was proceeded by 0 mM L-asp to control for changes in oocyte leak currents and followed by 1 mM to control for rundown or vice versa. Only oocytes that displayed delta currents bigger than 600 nA in the presence of saturating concentration of ligand were used. Each point in dose-response curves was calculated as follows: (current – leak)/(current at 1 mM L-asp – leak).

SUPPLEMENTARY MATERIALS

Supplementary material for this article is available at http://advances.sciencemag.org/cgi/content/full/7/10/eabf5814/DC1

View/request a protocol for this paper from *Bio-protocol*.

REFERENCES AND NOTES

1. R. J. Vandenberg, R. M. Ryan, Mechanisms of glutamate transport. *Physiol. Rev.* **93**, 1621–1657 (2013).
2. C. Grewer, A. Gameiro, T. Rauen, SLC1 glutamate transporters. *Pflugers Arch.* **466**, 3–24 (2014).
3. W. E. Bjorn-Yoshimoto, S. M. Underhill, The importance of the excitatory amino acid transporter 3 (EAAT3). *Neurochem. Int.* **98**, 4–18 (2016).
4. Y. Kanai, M. A. Hediger, Primary structure and functional characterization of a high-affinity glutamate transporter. *Nature* **360**, 467–471 (1992).
5. J. D. Rothstein, L. Martin, A. I. Levey, M. Dykes-Hoberg, L. Jin, D. Wu, N. Nash, R. W. Kuncl, Localization of neuronal and glial glutamate transporters. *Neuron* **13**, 713–725 (1994).
6. C. G. Bailey, R. M. Ryan, A. D. Thoeng, C. Ng, K. King, J. M. Vanslambrouck, C. Auray-Blais, R. J. Vandenberg, S. Broer, J. E. Rasko, Loss-of-function mutations in the glutamate transporter SLC1A1 cause human dicarboxylic aminoaciduria. *J. Clin. Invest.* **121**, 446–453 (2011).
7. P. Peghini, J. Janzen, W. Stoffel, Glutamate transporter EAAC-1-deficient mice develop dicarboxylic aminoaciduria and behavioral abnormalities but no neurodegeneration. *EMBO J.* **16**, 3822–3832 (1997).
8. P. D. Arnold, T. Sicard, E. Burroughs, M. A. Richter, J. L. Kennedy, Glutamate transporter gene SLC1A1 associated with obsessive-compulsive disorder. *Arch. Gen. Psychiatry* **63**, 769–776 (2006).
9. S. Holmseth, Y. Dehnes, Y. H. Huang, V. V. Follin-Arbelet, N. J. Grutle, M. N. Mylonakou, C. Plachez, Y. Zhou, D. N. Furness, D. E. Bergles, K. P. Lehre, N. C. Danbolt, The density of EAAC1 (EAAT3) glutamate transporters expressed by neurons in the mammalian CNS. *J. Neurosci.* **32**, 6000–6013 (2012).
10. J. D. Rothstein, M. Dykes-Hoberg, C. A. Pardo, L. A. Bristol, L. Jin, R. W. Kuncl, Y. Kanai, M. A. Hediger, Y. Wang, J. P. Schielke, D. F. Welty, Knockout of glutamate transporters reveals a major role for astroglial transport in excitotoxicity and clearance of glutamate. *Neuron* **16**, 675–686 (1996).
11. S. N. Rakhade, J. A. Loeb, Focal reduction of neuronal glutamate transporters in human neocortical epilepsy. *Epilepsia* **49**, 226–236 (2008).
12. R. E. McCullumsmith, J. H. Meador-Woodruff, Striatal excitatory amino acid transporter transcript expression in schizophrenia, bipolar disorder, and major depressive disorder. *Neuropsychopharmacology* **26**, 368–375 (2002).
13. H. Fujita, K. Sato, T. C. Wen, Y. Peng, M. Sakanaka, Differential expressions of glycine transporter 1 and three glutamate transporter mRNA in the hippocampus of gerbils with transient forebrain ischemia. *J. Cereb. Blood Flow Metab.* **19**, 604–615 (1999).
14. M. G. Bianchi, D. Bardelli, M. Chiu, O. Bussolati, Changes in the expression of the glutamate transporter EAAT3/EAAC1 in health and disease. *Cell. Mol. Life Sci.* **71**, 2001–2015 (2014).
15. N. Zerangue, M. P. Kavanaugh, Interaction of L-cysteine with a human excitatory amino acid transporter. *J. Physiol.* **493** (Pt 2), 419–423 (1996).
16. S. D. Watts, D. Torres-Salazar, C. B. Divito, S. G. Amara, Cysteine transport through excitatory amino acid transporter 3 (EAAT3). *PLOS ONE* **9**, e109245 (2014).
17. K. Aoyama, S. W. Suh, A. M. Hamby, J. Liu, W. Y. Chan, Y. Chen, R. A. Swanson, Neuronal glutathione deficiency and age-dependent neurodegeneration in the EAAC1 deficient mouse. *Nat. Neurosci.* **9**, 119–126 (2006).
18. J. I. Wadiche, S. G. Amara, M. P. Kavanaugh, Ion fluxes associated with excitatory amino acid transport. *Neuron* **15**, 721–728 (1995).
19. B. Billups, D. Rossi, D. Attwell, Anion conductance behavior of the glutamate uptake carrier in salamander retinal glial cells. *J. Neurosci.* **16**, 6722–6731 (1996).
20. R. J. Vandenberg, J. L. Arriza, S. G. Amara, M. P. Kavanaugh, Constitutive ion fluxes and substrate binding domains of human glutamate transporters. *J. Biol. Chem.* **270**, 17668–17671 (1995).
21. W. A. Fairman, R. J. Vandenberg, J. L. Arriza, M. P. Kavanaugh, S. G. Amara, An excitatory amino-acid transporter with properties of a ligand-gated chloride channel. *Nature* **375**, 599–603 (1995).
22. S. Eliasof, C. E. Jahr, Retinal glial cell glutamate transporter is coupled to an anionic conductance. *Proc. Natl. Acad. Sci. U.S.A.* **93**, 4153–4158 (1996).
23. N. Zerangue, M. P. Kavanaugh, Flux coupling in a neuronal glutamate transporter. *Nature* **383**, 634–637 (1996).
24. N. Watzke, E. Bamberg, C. Grewer, Early intermediates in the transport cycle of the neuronal excitatory amino acid carrier EAAC1. *J. Gen. Physiol.* **117**, 547–562 (2001).
25. L. Borre, B. I. Kanner, Coupled, but not uncoupled, fluxes in a neuronal glutamate transporter can be activated by lithium ions. *J. Biol. Chem.* **276**, 40396–40401 (2001).
26. N. Watzke, T. Rauen, E. Bamberg, C. Grewer, On the mechanism of proton transport by the neuronal excitatory amino acid carrier 1. *J. Gen. Physiol.* **116**, 609–622 (2000).
27. Z. Zhang, Z. Tao, A. Gameiro, S. Barcelona, S. Braams, T. Rauen, C. Grewer, Transport direction determines the kinetics of substrate transport by the glutamate transporter EAAC1. *Proc. Natl. Acad. Sci. U.S.A.* **104**, 18025–18030 (2007).
28. D. Yernool, O. Boudker, Y. Jin, E. Gouaux, Structure of a glutamate transporter homologue from *Pyrococcus horikoshii*. *Nature* **431**, 811–818 (2004).
29. O. Boudker, R. M. Ryan, D. Yernool, K. Shimamoto, E. Gouaux, Coupling substrate and ion binding to extracellular gate of a sodium-dependent aspartate transporter. *Nature* **445**, 387–393 (2007).
30. N. Reyes, C. Ginter, O. Boudker, Transport mechanism of a bacterial homologue of glutamate transporters. *Nature* **462**, 880–885 (2009).
31. A. Guskov, S. Jensen, I. Faustino, S. J. Marrink, D. J. Slotboom, Coupled binding mechanism of three sodium ions and aspartate in the glutamate transporter homologue GltTk. *Nat. Commun.* **7**, 13420 (2016).
32. J. C. Canul-Tec, R. Assal, E. Cirri, P. Legrand, S. Brier, J. Chamot-Rooke, N. Reyes, Structure and allosteric inhibition of excitatory amino acid transporter 1. *Nature* **544**, 446–451 (2017).

33. A. A. Garaeva, G. T. Oostergetel, C. Gati, A. Guskov, C. Paulino, D. J. Slotboom, Cryo-EM structure of the human neutral amino acid transporter ASCT2. *Nat. Struct. Mol. Biol.* **25**, 515–521 (2018).
34. X. Yu, O. Plotnikova, P. D. Bonin, T. A. Subashi, T. J. McLellan, D. Dumlao, Y. Che, Y. Y. Dong, E. P. Carpenter, G. M. West, X. Qiu, J. S. Culp, S. Han, Cryo-EM structures of the human glutamine transporter SLC1A5 (ASCT2) in the outward-facing conformation. *eLife* **8**, (2019).
35. C. Grewer, P. Balani, C. Weidenfeller, T. Bartusel, Z. Tao, T. Rauen, Individual subunits of the glutamate transporter EAAC1 homotrimer function independently of each other. *Biochemistry* **44**, 11913–11923 (2005).
36. G. P. Leary, E. F. Stone, D. C. Holley, M. P. Kavanaugh, The glutamate and chloride permeation pathways are colocalized in individual neuronal glutamate transporter subunits. *J. Neurosci.* **27**, 2938–2942 (2007).
37. H. P. Koch, R. L. Brown, H. P. Larsson, The glutamate-activated anion conductance in excitatory amino acid transporters is gated independently by the individual subunits. *J. Neurosci.* **27**, 2943–2947 (2007).
38. V. Arkhipova, A. Guskov, D. J. Slotboom, Structural ensemble of a glutamate transporter homologue in lipid nanodisc environment. *Nat. Commun.* **11**, 998 (2020).
39. X. Wang, O. Boudker, Large domain movements through the lipid bilayer mediate substrate release and inhibition of glutamate transporters. *eLife* **9**, e58417 (2020).
40. A. A. Garaeva, A. Guskov, D. J. Slotboom, C. Paulino, A one-gate elevator mechanism for the human neutral amino acid transporter ASCT2. *Nat. Commun.* **10**, 3427 (2019).
41. N. Reyes, S. Oh, O. Boudker, Binding thermodynamics of a glutamate transporter homolog. *Nat. Struct. Mol. Biol.* **20**, 634–640 (2013).
42. A. Bendahan, A. Armon, N. Madani, M. P. Kavanaugh, B. I. Kanner, Arginine 447 plays a pivotal role in substrate interactions in a neuronal glutamate transporter. *J. Biol. Chem.* **275**, 37436–37442 (2000).
43. S. Teichman, S. Qu, B. I. Kanner, Conserved asparagine residue located in binding pocket controls cation selectivity and substrate interactions in neuronal glutamate transporter. *J. Biol. Chem.* **287**, 17198–17205 (2012).
44. L. M. Levy, O. Warr, D. Attwell, Stoichiometry of the glial glutamate transporter GLT-1 expressed inducibly in a Chinese hamster ovary cell line selected for low endogenous Na+–dependent glutamate uptake. *J. Neurosci.* **18**, 9620–9628 (1998).
45. S. G. Owe, P. Marcaggi, D. Attwell, The ionic stoichiometry of the GLAST glutamate transporter in salamander retinal glia. *J. Physiol.* **577**, 591–599 (2006).
46. M. Groeneveld, D. J. Slotboom, Na+:aspartate coupling stoichiometry in the glutamate transporter homologue GltPh. *Biochemistry* **49**, 3511–3513 (2010).
47. Z. Huang, E. Tajkhorshid, Identification of the third Na+ site and the sequence of extracellular binding events in the glutamate transporter. *Biophys. J.* **99**, 1416–1425 (2010).
48. T. Bastug, G. Heinzelmann, S. Kuyucak, M. Salim, R. J. Vandenberg, R. M. Ryan, Position of the third Na+ site in the aspartate transporter GltPh and the human glutamate transporter, EAAT1. *PLOS ONE* **7**, e33058 (2012).
49. S. Oh, O. Boudker, Kinetic mechanism of coupled binding in sodium-aspartate symporter GltPh. *eLife* **7**, (2018).
50. Z. Tao, Z. Zhang, C. Grewer, Neutralization of the aspartic acid residue Asp-367, but not Asp-454, inhibits binding of Na+ to the glutamate-free form and cycling of the glutamate transporter EAAC1. *J. Biol. Chem.* **281**, 10263–10272 (2006).
51. G. Verdon, S. Oh, R. N. Serio, O. Boudker, Coupled ion binding and structural transitions along the transport cycle of glutamate transporters. *eLife* **3**, e02283 (2014).
52. E. A. Riederer, F. I. Valiyaveetil, Investigation of the allosteric coupling mechanism in a glutamate transporter homolog via unnatural amino acid mutagenesis. *Proc. Natl. Acad. Sci. U.S.A.* **116**, 15939–15946 (2019).
53. P. J. Focke, P. Moenne-Loccoz, H. P. Larsson, Opposite movement of the external gate of a glutamate transporter homolog upon binding cotransported sodium compared with substrate. *J. Neurosci.* **31**, 6255–6262 (2011).
54. D. Kortzak, C. Alleva, I. Weyand, D. Ewers, M. I. Zimmermann, A. Franzen, J. P. Machtens, C. Fahlke, Allosteric gate modulation confers K(+) coupling in glutamate transporters. *EMBO J.* **38**, e101468 (2019).
55. J. Wang, K. Zhang, P. Goyal, C. Grewer, Mechanism and potential sites of potassium interaction with glutamate transporters. *J. Gen. Physiol.* **152**, (2020).
56. C. Grewer, N. Watzke, T. Rauen, A. Bicho, Is the glutamate residue Glu-373 the proton acceptor of the excitatory amino acid carrier 1? *J. Biol. Chem.* **278**, 2585–2592 (2003).
57. B. I. Kanner, M. P. Kavanaugh, A. Bendahan, Molecular characterization of substrate-binding sites in the glutamate transporter family. *Biochem. Soc. Trans.* **29**, 707–710 (2001).
58. M. H. Olsson, C. R. Sondergaard, M. Rostkowski, J. H. Jensen, PROPKA3: Consistent treatment of internal and surface residues in empirical pK_a predictions. *J. Chem. Theory Comput.* **7**, 525–537 (2010).
59. G. Heinzelmann, S. Kuyucak, Molecular dynamics simulations elucidate the mechanism of proton transport in the glutamate transporter EAAT3. *Biophys. J.* **106**, 2675–2683 (2014).
60. C. Grewer, N. Watzke, M. Wiessner, T. Rauen, Glutamate translocation of the neuronal glutamate transporter EAAC1 occurs within milliseconds. *Proc. Natl. Acad. Sci. U.S.A.* **97**, 9706–9711 (2000).
61. D. N. Mastronarde, Automated electron microscope tomography using robust prediction of specimen movements. *J. Struct. Biol.* **152**, 36–51 (2005).
62. M. Schorb, I. Haberbosch, W. J. H. Hagen, Y. Schwab, D. N. Mastronarde, Software tools for automated transmission electron microscopy. *Nat. Methods* **16**, 471–477 (2019).
63. S. Q. Zheng, E. Palovcak, J. P. Armache, K. A. Verba, Y. Cheng, D. A. Agard, MotionCor2: Anisotropic correction of beam-induced motion for improved cryo-electron microscopy. *Nat. Methods* **14**, 331–332 (2017).
64. K. Zhang, Gctf: Real-time CTF determination and correction. *J. Struct. Biol.* **193**, 1–12 (2016).
65. S. H. Scheres, RELION: Implementation of a Bayesian approach to cryo-EM structure determination. *J. Struct. Biol.* **180**, 519–530 (2012).
66. A. Rohou, N. Grigorieff, CTFFIND4: Fast and accurate defocus estimation from electron micrographs. *J. Struct. Biol.* **192**, 216–221 (2015).
67. P. Emsley, B. Lohkamp, W. G. Scott, K. Cowtan, Features and development of Coot. *Acta Crystallogr. D Biol. Crystallogr.* **66**, 486–501 (2010).
68. P. D. Adams, P. V. Afonine, G. Bunkoczi, V. B. Chen, I. W. Davis, N. Echols, J. J. Headd, L. W. Hung, G. J. Kapral, R. W. Grosse-Kunstleve, A. J. McCoy, N. W. Moriarty, R. Oeffner, R. J. Read, D. C. Richardson, J. S. Richardson, T. C. Terwilliger, P. H. Zwart, PHENIX: A comprehensive Python-based system for macromolecular structure solution. *Acta Crystallogr. D Biol. Crystallogr.* **66**, 213–221 (2010).
69. A. Amunts, A. Brown, X. C. Bai, J. L. Llacer, T. Hussain, P. Emsley, F. Long, G. Murshudov, S. H. W. Scheres, V. Ramakrishnan, Structure of the yeast mitochondrial large ribosomal subunit. *Science* **343**, 1485–1489 (2014).
70. E. F. Pettersen, T. D. Goddard, C. C. Huang, G. S. Couch, D. M. Greenblatt, E. C. Meng, T. E. Ferrin, UCSF Chimera–A visualization system for exploratory research and analysis. *J. Comput. Chem.* **25**, 1605–1612 (2004).
71. A. Bazzone, M. Barthmes, K. Fendler, SSM-based electrophysiology for transporter research. *Methods Enzymol.* **594**, 31–83 (2017).
72. R. Krause, N. Watzke, B. Kelety, W. Dorner, K. Fendler, An automatic electrophysiological assay for the neuronal glutamate transporter mEAAC1. *J. Neurosci. Methods* **177**, 131–141 (2009).
73. M. D. Winn, C. C. Ballard, K. D. Cowtan, E. J. Dodson, P. Emsley, P. R. Evans, R. M. Keegan, E. B. Krissinel, A. G. Leslie, A. McCoy, S. J. McNicholas, G. N. Murshudov, N. S. Pannu, E. A. Potterton, H. R. Powell, R. J. Read, A. Vagin, K. S. Wilson, Overview of the CCP4 suite and current developments. *Acta Crystallogr. D Biol. Crystallogr.* **67**, 235–242 (2011).

Acknowledgments: We thank the Weill Cornell Medicine mass spectrometry facility for verifying the protein identity and the NYSBC Simons EM center for access to the microscopes. We thank M. Kopylov at NYSBC Simons EM center for assistance with data collection and S. Wang from MSKCC for the initial scripts for particle sorting. We thank X. Wang and D. Ciftci for discussions. **Funding:** This study was supported by National Institute of Neurological Disorders and Stroke R01NS064357 to O.B. **Author contributions:** B.Q. and O.B. designed the experiments. B.Q. performed the experiments, processed and analyzed data, and refined the molecular models. D.M. optimized grid preparation and performed preliminary data processing. D.M. and B.Q. collected cryo-EM data, with Z.Y. overseeing all aspects of the microscope operation. B.Q. and E.F. performed electrophysiology experiments. B.Q. and O.B. wrote the manuscript with input from all authors. **Competing interests:** The authors declare that they have no competing financial interests. **Data and materials availability:** Atomic coordinates for the cryo-EM structures have been deposited in the Protein Data Bank under accession codes 6X2L, 6X2Z, 6X3E, and 6X3F. The corresponding cryo-EM maps have been deposited in the Electron Microscopy Data Bank (EMDB) under accession codes 22011, 22014, 22020, and 22021, respectively. Additional cryo-EM maps have been deposited into EMDB under accession code 22023. All data needed to evaluate the conclusions in the paper are present in the paper and/or the Supplementary Materials. Additional data related to this paper may be requested from the authors.

Submitted 5 November 2020
Accepted 19 January 2021
Published 3 March 2021
10.1126/sciadv.abf5814

Citation: B. Qiu, D. Matthies, E. Fortea, Z. Yu, O. Boudker, Cryo-EM structures of excitatory amino acid transporter 3 visualize coupled substrate, sodium, and proton binding and transport. *Sci. Adv.* **7**, eabf5814 (2021).